Electrically-pumped compact hybrid silicon microring lasers for optical interconnects

Di Liang,[1]* Marco Fiorentino,[2] Tadashi Okumura,[1] Hsu-Hao Chang,[1] Daryl T. Spencer,[1] Ying-Hao Kuo,[1] Alexander W. Fang,[1] Daoxin Dai,[1] Raymond G. Beausoleil,[2] and John E. Bowers[1]

[1]*Department of Electrical and Computer Engineering, University of California, Santa Barbara, CA 93106, USA*
[2]*Information and Quantum Systems Lab, Hewlett Packard Laboratories, Palo Alto, CA 94304, USA*
**dliang@ece.ucsb.edu*

Abstract: We demonstrate an electrically-pumped hybrid silicon microring laser fabricated by a self-aligned process. The compact structure (D = 50 μm) and small electrical and optical losses result in lasing threshold as low as 5.4 mA and up to 65 °C operation temperature in continuous-wave (cw) mode. The spectrum is single mode with large extinction ratio and small linewidth observed. Application as on-chip optical interconnects is discussed from a system perspective.

OCIS codes: (140.5960) Semiconductor lasers; (140.3948) Microcavity devices.

References and links

1. A. S.-H. Liao, and S. Wang, "Semiconductor injection lasers with a circular resonator," Appl. Phys. Lett. **36**(10), 801–803 (1980).
2. A. M. Prabhu, A. Tsay, H. Zhanghua, and V. Vien, "Ultracompact SOI Microring Add/Drop Filter With Wide Bandwidth and Wide FSR," IEEE Photon. Technol. Lett. **21**(10), 651–653 (2009).
3. A. W. Poon, X. S. Luo, F. Xu, and H. Chen, "Cascaded Microresonator-Based Matrix Switch for Silicon On-Chip Optical Interconnection," Proc. IEEE **97**(7), 1216–1238 (2009).
4. S. Wang, A. Ramachandran, and S.-J. Ja, "Integrated microring resonator biosensors for monitoring cell growth and detectionr of toxic chemicals in water," Biosens. Bioelectron. **24**(10), 3061–3066 (2009).
5. Q. Xu, B. Schmidt, S. Pradhan, and M. Lipson, "Micrometre-scale silicon electro-optic modulator," Nature **435**(7040), 325–327 (2005).
6. F. Xia, L. Sekaric, and Y. Vlasov, "Ultracompact optical buffers on a silicon chip," Nat. Photonics **1**(1), 65–71 (2007).
7. H. Park, A. W. Fang, S. Kodama, and J. E. Bowers, "Hybrid silicon evanescent laser fabricated with a silicon waveguide and III-V offset quantum wells," Opt. Express **13**(23), 9460–9464 (2005).
8. A. W. Fang, H. Park, O. Cohen, R. Jones, M. J. Paniccia, and J. E. Bowers, "Electrically pumped hybrid AlGaInAs-silicon evanescent laser," Opt. Express **14**(20), 9203–9210 (2006).
9. A. W. Fang, R. Jones, H. Park, O. Cohen, O. Raday, M. J. Paniccia, and J. E. Bowers, "Integrated AlGaInAs-silicon evanescent race track laser and photodetector," Opt. Express **15**(5), 2315–2322 (2007).
10. A. W. Fang, E. Lively, Y.-H. Kuo, D. Liang, and J. E. Bowers, "A distributed feedback silicon evanescent laser," Opt. Express **16**(7), 4413–4419 (2008).
11. J. Van Campenhout, P. Rojo Romeo, P. Regreny, C. Seassal, D. Van Thourhout, S. Verstuyft, L. Di Cioccio, J. M. Fedeli, C. Lagahe, and R. Baets, "Electrically pumped InP-based microdisk lasers integrated with a nanophotonic silicon-on-insulator waveguide circuit," Opt. Express **15**(11), 6744–6749 (2007).
12. D. Liang, M. Fiorentino, A. W. Fang, D. Dai, Y.-H. Kuo, R. G. Beausoleil, and J. E. Bowers, "An Optically-Pumped Silicon Evanescent Microring Resonator Laser," in *The 6th IEEE international conference on Group IV Photonics*, 2009), paper FA5.
13. K. K. Lee, D. R. Lim, H.-C. Luan, A. Agarwal, J. Foresi, and L. C. Kimerling, "Effect of size and roughness on light transmission in a Si/SiO2 waveguide: experiments and model," Appl. Phys. Lett. **77**(11), 1617–1619 (2000).
14. H. Park, A. W. Fang, R. Jones, O. Cohen, O. Raday, M. N. Sysak, M. J. Paniccia, and J. E. Bowers, "A hybrid AlGaInAs-silicon evanescent waveguide photodetector," Opt. Express **15**(10), 6044–6052 (2007).
15. D. Liang, and J. E. Bowers, "Highly Efficient Vertical Outgassing Channels for Low-Temperature InP-to-Silicon Direct Wafer Bonding on the Silicon-On-Insulator (SOI) Substrate," J. Vac. Sci. Technol. B **26**(4), 1560–1568 (2008).
16. Q. Xu, D. Fattal, and R. G. Beausoleil, "Silicon microring resonators with 1.5-microm radius," Opt. Express **16**(6), 4309–4315 (2008).
17. G. Mezosi, M. J. Strain, S. Furst, Z. Wang, S. Yu, and M. Sorel, "Unidirectional Bistability in AlGaInAs Microring and Microdisk Semiconductor Lasers," IEEE Photon. Technol. Lett. **21**(2), 88–90 (2009).

#115497 - $15.00 USD Received 10 Aug 2009; revised 14 Oct 2009; accepted 20 Oct 2009; published 23 Oct 2009

18. G. Franz, "Damage in III/V semiconductors caused by hard- and soft-etching plasmas," J. Vac. Sci. Technol. A **19**(3), 762–772 (2001).
19. S. Bull, A. V. Andrianov, I. Harrison, and E. C. Larkins, "The study of strain and defects in high power laser diodes by spectroscopically resolved photoluminescence microscopy," Eur. Phys. J. Appl. Phys. **27**(1-3), 469–473 (2004).
20. A. Boudjani, B. Sieber, F. Cleton, and A. Rudra, "Cl and EBIC analysis of a p+-InGaAs/n-InGaAs/n-InP/n+-InP heterostructure," Mater. Sci. Eng. B **42**(1-3), 192–198 (1996).
21. J.-T. Lim, J.-G. Choi, S. K. Noh, K.-C. Je, S.-Y. Yim, and S.-H. Park, "Nondestructive Photoacoustic Measurement of Doping Densities in Bulk GaAs," Jpn. J. Appl. Phys. **46**(12), 7888–7891 (2007).
22. U. Schade, S. Kollakowski, E. H. Böttcher, and D. Bimberg, "Improved performance of large-area InP/InGaAs metal-semiconductor-metal photodetectors by sulfur passivation," Appl. Phys. Lett. **64**(11), 1389–1391 (1994).
23. L. A. Coldren, and S. W. Corzine, *Diode Lasers and Photonic Integrated Circuits* (Wiley-Interscience, New York, USA, 1995).
24. M. Sorel, P. J. R. Laybourn, G. Giuliani, and S. Donati, "Unidirectional bistability in semiconductor waveguide ring lasers," Appl. Phys. Lett. **80**(17), 3051–3053 (2002).
25. A. W. Fang, B. R. Koch, R. Jones, E. Lively, Di Liang, Ying-Hao Kuo, and J. E. Bowers, "A Distributed Bragg Reflector Silicon Evanescent Laser," IEEE Photon. Technol. Lett. **20**(20), 1667–1669 (2008).
26. www.zarlink.com, www.finisar.com, www.luxtera.com, www.emcore.com
27. D. M. Taylor, C. R. Bennett, T. J. Shepherd, L. F. Michaille, M. D. Nielsen, and H. R. Simonsen, "Demonstration of multi-core photonic crystal fibre in an optical interconnect," Electron. Lett. **42**(6), 331–332 (2006).
28. D. Taillaert, W. Bogaerts, P. Bienstman, T. F. Krauss, P. Van Daele, I. Moerman, S. Verstuyft, K. De Mesel, and R. Baets, "An out-of-plane grating coupler for efficient butt-coupling between compact planar waveguides and single-mode fibers," IEEE J. Quantum Electron. **38**(7), 949–955 (2002).
29. J. Song, Q. Fang, S. H. Tao, M. B. Yu, G. Q. Lo, and D. L. Kwong, "Passive ring-assisted Mach-Zehnder interleaver on silicon-on-insulator," Opt. Express **16**(12), 8359–8365 (2008).
30. D. M. Taylor, and T. J. Shepherd, (personal communication, 2008).

1. Introduction

Diode lasers with ring or disk resonator geometries are one of the most attractive on-chip light sources for photonic integrated circuits (PICs) since their inherent traveling wave operation nature requires no gratings or Fabry-Perot (FP) facets for optical feedback [1]. As a type of multi-functional component, compact passive microring resonators have been used extensively on Si substrates for wavelength division multiplexing (WDM) add-drop filters/routers [2], switches [3], sensors [4], modulator [5] and buffers [6]. A microring-based Si transmitter is possible for on-chip optical interconnect application if a laser can be integrated as well. Practical use requires power efficient, continuous-wave (cw) operation, high-speed direct modulation and operation at evaluated temperature, which are analyzed here.

The hybrid silicon platform (HSP) [7, 8] is a promising approach to enable robust active components on a complementary metal-oxide semiconductor (CMOS)-compatible Si platform. The first on-chip light source fabricated on HSP employs a racetrack ring resonator geometry [9] but retains the same cross-sectional structure as that of straight Fabry-Perot (FP) ones [8]. It consisted of a 1-2 μm wide SOI waveguide covered by a wider III-V mesa, which leads to a hybrid mode that spans both III-V and Si. The poor lateral optical confinement for the hybrid optical mode requires the bend radius ≥100 μm such that resulting excess bending loss is smaller than available gain. The long cavity length of ~2.6 mm and modal mismatch at the straight and bent waveguide sections cause relatively high threshold current of ~175 mA [9]. More recently distributed feedback (DFB) hybrid silicon lasers achieved up to 7× threshold decrease with 340 μm long grating region [10]. Further reduction in threshold and device footprint was demonstrated by a 7.5 μm-diameter disk laser integrated on SOI substrate with polymer-based wafer bonding technique [11], thus showing the potential to realize on-chip Si light sources with low power consumption and high-speed direct modulation using a compact micro-ring/disk structure. Recently, we developed optically-pumped hybrid silicon microring lasers with small diameters of 15 and 25 μm [12]. In these lasers we measured a threshold carrier density of ~2.5×10^{18} cm^{-3} indicating low optical and electrical losses. In this paper we demonstrate the electrically-driven version of this compact microring laser and discuss their potential application for optical interconnects from a system perspective.

#115497 - $15.00 USD Received 10 Aug 2009; revised 14 Oct 2009; accepted 20 Oct 2009; published 23 Oct 2009

2. Device design and fabrication

Figure 1(a) shows the schematic of the hybrid silicon microring laser. The laser comprises an III-V ring resonator on top of a silicon disk with the same diameter. The fundamental whisper-gallery mode shifts towards the resonator edge as shown by a Beam Propagation Method (BPM) simulated mode profile in the inset of Fig. 1(a). The III-V epitaxial structure includes five periods of InAlGaAs-based, quantum wells (λ_g=1.51 μm) plus a p-doped 50 nm-thick InAlGaAs separate confinement heterostructure (SCH) layer are sandwiched by a 110 nm-thick n-doped InP contact layer and a p-doped 1.5 μm-thick InP cladding layer. This structure is bonded on top of a SOI wafer with a 350 nm-thick silicon device layer, resulting in confinement factors of 15.2% and 51.7% in active region and silicon, respectively. A SOI bus waveguide w_{WG}=0.6, 0.8 and 1 μm-wide, 25 μm-long is s=50-500 nm away from the resonator, as shown in Fig. 1. The SOI waveguide is then tapered up to 1.5 μm through two 105 μm long tapers to minimize the sidewall-induced scattering loss [13], resulting a 235 μm-long bus waveguide to guide coupled light to two integrated photodetectors. The taper-shaped photodetectors with a total length of 180 μm are employed to adiabatically transform the mode from the passive SOI waveguide to hybrid waveguide detectors with low coupling loss and small reflection [14].

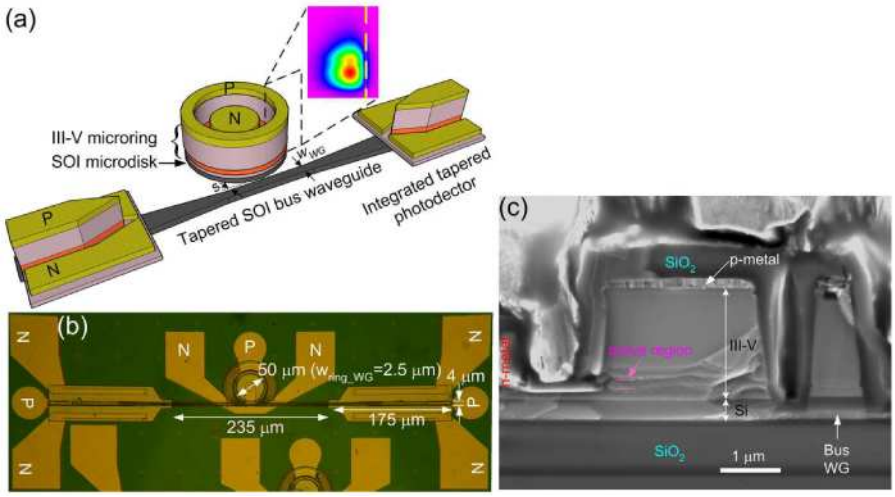

Fig. 1. (a) Schematic of compact hybrid silicon ring resonator laser with BPM mode profile and integrated, tapered photodetectors. Variables of coupling gap s and bus waveguide width w_{WG} are labeled. (b) The microscopic image of a finished device with critical dimension labeled. (c) SEM cross-sectional image of the evanescent point coupler.

Figure 2 schematically highlights the critical processing steps in the device fabrication. The fabrication starts by patterning 1.5 μm-wide bus waveguides on the SOI substrate where tapered photodetectors will sit. Vertical outgassing channels are formed in the same step to allow the transfer of a high-quality III-V epitaxial layer onto silicon through a low-temperature O_2 plasma-assisted wafer bonding process [15]. After bonding the InP carrier substrate is selectively removed and the p-type contact metal (W/Pd/Ti/Pd) is deposited on the p-InGaAs contact layer by E-beam evaporation (Pd/Ti/Pd) and sputtering (W). The metal is coated with a SiO_2 hardmask using plasma-enhanced chemical vapor deposition (PECVD). The narrow bus waveguide with tapered sections and the 50 μm diameter disk resonator are patterned in a resist layer using E-beam lithography (Fig. 2(a)). Successive inductively coupled plasma (ICP) reactive ion etching steps are used to transfer the pattern to the SiO_2 hardmask, p-metal, and the ~2 μm-thick III-V all the way through top silicon layer. This process is highly anisotropic and gives smooth sidewall profile (Fig. 2(b)) for tight dimension control and low scattering loss. We measured an etch angle of ~86°in the scanning electron microscope in Fig. 1(c). This is, therefore, a self-aligned process to avoid misalignment

#115497 - $15.00 USD Received 10 Aug 2009; revised 14 Oct 2009; accepted 20 Oct 2009; published 23 Oct 2009

between III-V ring and Si disk resonators. After passivating the etch-exposed III-V sidewall with PECVD SiO_2, a 45 μm diameter open circular area inside the disk is defined by conventional projection lithography (Fig. 2(c)). We then apply dry-etch steps to remove PECVD SiO_2, metal, and InP to reach the active region which is selectively removed by H_2SO_4-based solution, resulting in the exposure of the n-type InP contact layer (Fig. 2(d)). The III-V material, with the exception of a thin n-InP layer on top of Si bus waveguide, is removed in this step. These steps form a III-V ring resonator with a 2.5 μm waveguide width. In contrast to the typical silicon hybrid device structure, this deep-etched interface allows much stronger lateral optical confinement ($\Delta n \approx 2$). After depositing another layer of PECVD SiO_2 to passivate the inner sidewall of the ring, the n-metal (Ni/Ge/Au/Ni/Au) is then formed onto the n-contact InP layer inside the ring and near the photodetector mesa through photolithography and lift-off (Fig. 2(e)). After metallization and final dielectric passivation, the thick probe metal pads are deposited (Fig. 2(f)).

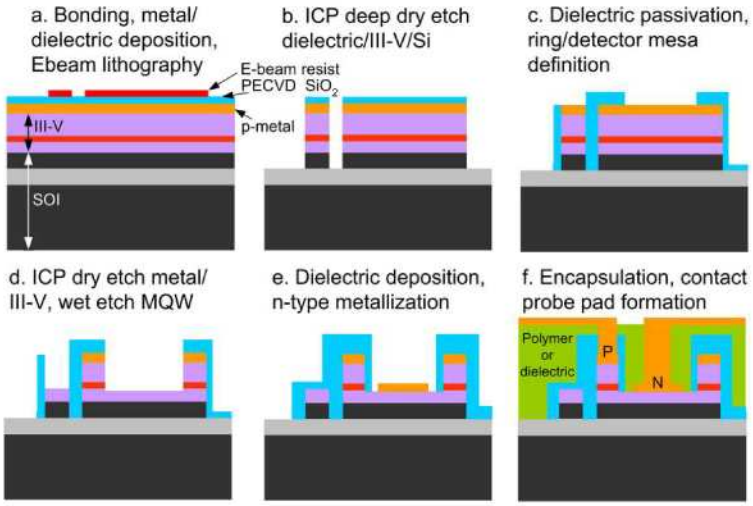

Fig. 2. Schematic of critical fabrication steps (not to scale).

3. Experimental results

Figure 3 shows the typical cw, temperature-dependent light-current (LI) characteristic of devices with (a) 150 nm and (b) 250 nm coupling gaps and w_{WG}=0.6 μm bus waveguide. Devices with III-V junction side up sit on a copper stage whose temperature (labeled next to each LI curve) is actively controlled. For coupling gap s=150 and 250 nm, the minimum threshold currents are 8.37 and 5.97 mA at 10 °C, respectively. They correspond to the respective threshold current densities of 2.02 and 1.43 kA/cm^2, assuming uniform carrier distribution in the w_{ring_WG}=2.8 μm active region. There numbers are similar to that of previously demonstrated FP (2 kA/cm^2) [8], racetrack (1.7 kA/cm^2) [9] and DFB (1.4 kA/cm^2) [10] lasers. Threshold voltages measured at room temperature (RT=20 °C) are 1.39 V (I_{th}=9.56 mA) and 1.33 V (I_{th}=7.61 mA) for devices in Figs. 5(a) and 5(b), respectively, which lead to laser turn-on powers of 13.29 mW and 10.12 mW. The average series resistance of 24 devices is 31.42 Ω at RT. Devices of s=150 and 250 nm lase up to a stage temperatures of 40 and 65 °C, respectively. The cw LI measurement stops at 25 mA typically in order to avoid excessive device heating.

Figure 3(c) summarizes the threshold currents for different bus waveguide widths as a function of coupling gap at RT. As the coupling gap increases from 50 to 250 nm, outcoupling coefficient equivalent to mirror loss for straight devices decreases exponentially from 0.03 to 1.28×10^{-5} based on 2-dimentional (2D) finite-difference time-domain (FDTD) simulation. However, the threshold follows a linear or weak exponential decay, resulting in

#115497 - $15.00 USD Received 10 Aug 2009; revised 14 Oct 2009; accepted 20 Oct 2009; published 23 Oct 2009

only ~2.4× reduction to s=250 nm. It indicates internal cavity loss comparable or even larger than the distributed outcoupling loss at s=50 nm, and dominating the total round-trip loss for weak coupling (s=50 nm). Lower threshold for large s is likely to be from the slightly lower internal cavity loss since narrow trench (i.e., small s) results in dry etch lag and poor PECVD SiO_2 sidewall coverage, introducing higher modal loss at evanescent point coupling region. We detect lasing in devices with s=500 nm by monitoring the infrared image since the photodetectors are unable to capture the lasing signal due to negligible outcoupling from the microrings and large waveguide loss. No lasing at RT is observed for devices with w_{WG}=800 and 1000 nm when s=50 nm. We measure higher thresholds are for devices with s=150 nm and bus waveguide widths w_{WG}=800 and 1000 nm. FDTD simulation shows higher outcoupling coefficient for wider bus waveguides, however, the cavity Q-factor also decreases dramatically if bus waveguide is wider than modal width in the microring cavity due to phase mismatch between ring and bus waveguide [16]. We attribute the absence of lasing for s=50 nm and higher threshold for s=150 nm for bus waveguide widths of 800 and 1000 nm to higher outcoupling and higher internal cavity losses.

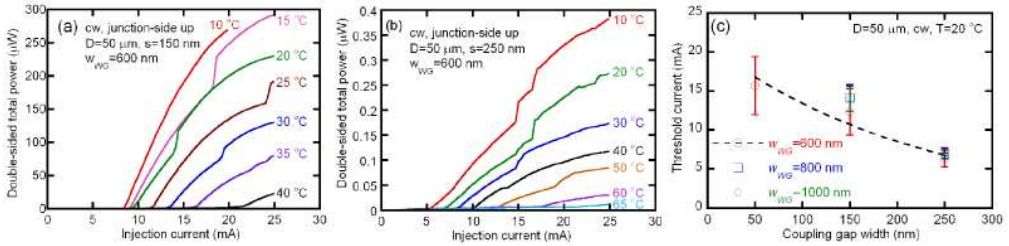

Fig. 3. LI characteristic of microring lasers with coupling gap (a) s=150 nm and (b) s=250 nm at various stage temperatures. (c) Threshold currents of different bus waveguide widths as a function of coupling gap width.

The output power in Fig. 3 is the sum of the photocurrent measured at both photodetectors. The photodetector responsivity is assumed to be 1 A/W therefore the laser power values are conservatively estimated [14]. As mentioned in the fabrication section, we failed to remove III-V epitaxial layers on the Si bus waveguide, resulting in a 235 μm long saturable absorber region. In addition to this substantial power loss from band-to-band absorption, free carrier absorption (FCA) and scattering loss also contribute to reduce the measured photocurrent. A column of devices with asymmetric photodetector position (i.e., with the right photodetectors 300 μm away from the laser) is used to estimate the total bus waveguide loss. We dice off the right photodetectors leaving the lossy 235 μm long bus waveguide intact and measure the amplified spontaneous emission (ASE) output from the left photodetector which is forward biased at 1-1.5 V. We then compare this output with the ASE from a photodetector at the same bias, which doesn't go through the bus waveguide region. The coupling gap s is 500 nm in this measurement to avoid the coupling to the microring. From these measurements, we conservatively estimate the power loss to be 7 dB, corresponding to a 70 cm^{-1} waveguide loss, with assumption that both photodetectors have the same ASE efficiency and suffer identical coupling losses. Diode currents of both photodetectors are similar for identical biases, indicating similar ASE efficiency. Theoretical models give losses of ~3.37 cm^{-1} and ~5.77 cm^{-1} for free carrier absorption and scattering loss, respectively. These results were obtained assuming a 45% confinement factor in III-V and RMS sidewall roughness of 60 nm. Based on these estimates we believe that the output power would be at least 5 × higher if the active region and InP cladding were removed.

We attribute the kinks in the LI curves to a combination effect of bidirectional instability, and saturable absorption in the bus waveguide because they tend to appear at the similar power levels for different stage temperatures. When outcoupling is small and output is low (e.g., Fig. 3(b)), a small back reflection either from the bus waveguide/photodetector junctions or from the evanescent point coupler cannot be negligible. This leads to the coupling of

#115497 - $15.00 USD Received 10 Aug 2009; revised 14 Oct 2009; accepted 20 Oct 2009; published 23 Oct 2009

transverse modes as well as of clock-wise (CW) and counter-clock-wise CCW) lasing modes [17], and subsequently extra kinks in LI curves.

In contrast to previously demonstrated devices on HSP where the current channel is defined by proton implantation [8], the deeply-etched structure in this work poses a concern of the dry etch-exposed active region sidewall at the outer circumference of the microring. For a typical ridge waveguide lasers, the mesa etch stops above the active region to avoid exposing the active region. In the situations where active region needs to be exposed (e.g., vertical cavity surface-emitting lasers(VCSEL)), wet etch is preferable because dry etch causes more severe lattice damage, consequently generating more non-radiative recombination centers at the interface [18]. This creates a current leakage path at the interfaces of the active region with exposed surfaces thus increasing the threshold current, reducing the differential quantum efficiency, and inducing early device degradation. This effect is even more detrimental for narrow stripe geometry (i.e., this work) since the ratio of exposed surface-to-active region volume is high. Instead of employing conventional methods (e.g., time-resolved PL [19], electron beam induced current [20], or photoacoustic measurements [21]) to locate the defects and determine the non-radiative recombination velocity at the deep-etched III-V interface on the Si substrate, we studied the leakage current of photodetectors and lasers in reverse bias condition. Since only is the laser active region at outer circumference exposed by dry etch while active region at inner circumference and on photodetectors is exposed by wet etch, comparison of reverse bias dark current density for lasers and photodetectors allows qualitative and straightforward estimation of the leakage induced by dry-etching. Owing to the difference in the area of active regions for lasers and photodetectors, we define a one-dimensional (1D) dark current density J as

$$J = \frac{I}{L} \tag{1}$$

where I and L are dark current and the length of exposed active region, respectively. Here we assume that reserve bias saturation current in the diode region far from sidewall is negligibly small, i.e., only leakage current at the sidewall contributes to measured dark current. Therefore, we can write dark current for lasers I_l and photodetectors I_p as:

$$I_l = J_l L_l = J_o L_o + J_i L_i \tag{2}$$

$$I_p = J_p L_p \tag{3}$$

where J_o (J_i) and L_o (L_i) are dark current densities and exposed active region length at the ring outer (inner) sidewalls, respectively. Same definition applies to parameters for photodetectors with subscript "p". It is valid to assume that $J_i = J_p$ since active region at inner ring and photodetector mesa are exposed simultaneously with same wet etch. Plugging (3) into (2), we then obtain the ratio between the leakage current densities for dry etch and wet etch surfaces:

$$\frac{J_o}{J_i} = \frac{I_l L_p - L_l I_p}{L_o I_p} \tag{4}$$

#115497 - $15.00 USD Received 10 Aug 2009; revised 14 Oct 2009; accepted 20 Oct 2009; published 23 Oct 2009

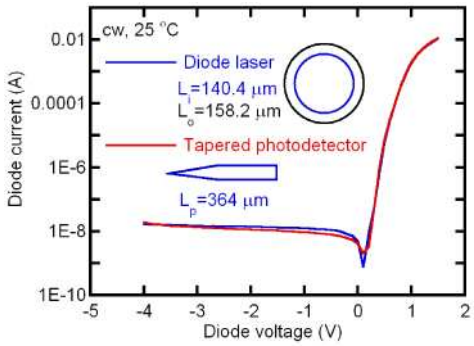

Fig. 4. Typical IV characteristics of a microring laser and one of its on-chip photodetectors. The length of exposed active region for laser and photodetector are shown in the inset. Blue and black present wet and dry etch defined interface.

Figure 4 shows typical current-voltage (IV) curves for a microring laser and a photodetector. Similar performance in both forward and reverse bias region exhibits comparable leakage current. The length of exposed active region for laser and photodetector are shown in the inset of Fig. 7, where blue and black lines represent wet and dry etch interfaces, respectively. If we take the angle of the dry etch surface into consideration, the inner and outer diameters of the microring are 44.7 and 50.3 μm, respectively. The measured dark current average values (its standard deviation) for 20 lasers and 24 photodetectors are 13.5 (10.3) and 7.6 (2.8) nA. Both lasers and photodetectors have dark currents in nA range. Plugging the average dark current values into Eq. (4), we obtain J_o/J_i=3.22, meaning that the leakage current at a dry-etch interface is 3.22 larger, per unit length, than a wet etch surface. The larger dark current standard deviation for lasers also indicates performance variation caused by the dry etched interface. However, this qualitative study shows that surface recombination at the dry etch-exposed active region does not significantly compromise device operation. The typical 2D dark current densities at −3 V for lasers and photodetectors are 32.39 and 15.46 pA/μm^2, respectively. These values are comparable to the values obtained from devices with special surface treatment [22]. Low intrinsic surface recombination velocity for InP-based semiconductors, well-controlled ICP dry etch, and good PECVD dielectric passivation all contribute to good interface condition for our deep-etched, narrow mesa structure.

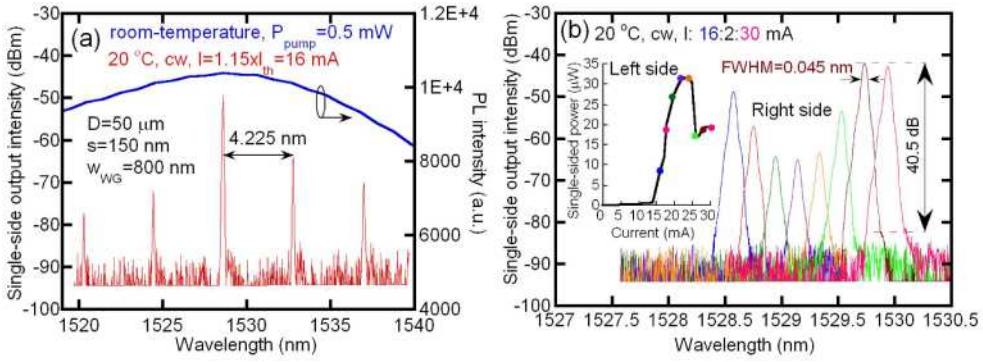

Fig. 5. (a) Spectrum measured at cw injection current of 16 mA (1.15×I_{th}) compared with photoluminescence result. (b) Spectra of primary lasing peak 16 to 30 mA cw current. Inset: LI curve measured from the photodetector on the left hand side. The color dots in the LI curve highlights the corresponding spectrum taken at the same current but with different laser emission direction.

Figure 5 shows the spectrum of a laser, the spectrum was measured by fiber coupling the output of a cleaved waveguide. The broadband spectrum in Fig. 5(a) shows that multiple

#115497 - $15.00 USD Received 10 Aug 2009; revised 14 Oct 2009; accepted 20 Oct 2009; published 23 Oct 2009

longitudinal cavity modes lase when device is driven at 16 mA ($1.15\times I_{th}$) at RT. The blue trace shows the photoluminescence (PL) spectrum measured by exciting a device without top InGaAs contact layer with a 0.5 mW 980 nm source at RT. Notice that the primary lasing peak is aligned with the PL maximum at 1528.57 nm. The free spectral range (FSR) is 4.2± 0.05 nm ((0.1 nm resolution for broadand sweep). Theoretical FSR value can be calculated from $FSR=\lambda_0^2/(n_g \pi D)$ [23] where λ_0, n_g are laser vacuum wavelength and group index, respectively, and πD is round-trip modal length. According to the FDTD simulation for the fundamental mode n_g=3.462 and D=49.77 μm and the FSR is 4.32 nm which agrees with the experimental data very well. A unique characteristic of disk/ring resonator lasers, unidirectional bistability [24], is also noticeable by comparing the peak intensity change in Fig. 5(b) and inset LI curve in it. The LI curve records the CW laser emission while the peak intensity change represents the output power variation of CCW lasing. It is clearly seen that for currents around 20 mA the primary lasing direction switches from CW to CCW.

While characterization of the dynamic properties of our devices is under development, Fig. 6 shows the calculated 3 dB bandwidth for injection current 10, 20 and 30 mA as a function of device diameter (cavity length). Previously FP and racetrack ring devices have shown ~50% injection efficiency, 1500 cm^{-1} material gain and 15 cm^{-1} modal loss. The racetrack devices, however have lower surface recombination and scattering losses and better carrier/optical mode overlap compared with the devices under study here. We therefore used a conservative estimate of the parameters including 30% injection efficiency, 1200 cm^{-1} material gain, 30 cm^{-1} modal loss and 3% outcoupling coefficient. These estimates result in ~5 mA threshold current for a 50 μm microring laser. No thermal effect is taken into account in this calculation. In order to achieve 3 dB bandwidth of 10 GHz, 50 μm diameter device needs to be driven with 20 mA bias current, i.e., $4\times I_{th}$. Devices in Fig. 4 demonstrate the capacity to operate at $4\times I_{th}$ without serious thermal roll-over. Devices with smaller dimension have smaller threshold and require less injection current to reach 10 GHz 3 dB bandwidth. As a reference, a DBR laser with 600 μm-long gain region fabricated on the same HSP has shown experimentally a ~2.5 GHz 3 dB bandwidth for a 105-mA ($1.6\times I_{th}$) bias current (black dot in Fig. 6). These same devices have shown 4 Gbit/sec data transmission for a bias of $\sim 2\times I_{th}$ [25]. Clearly, employing short cavity devices (e.g., microring lasers) is an efficient approach to further increase the direct modulation bandwidth without sacrificing low power dissipation. Increased thermal impedance poses a major obstacle for all compact devices.

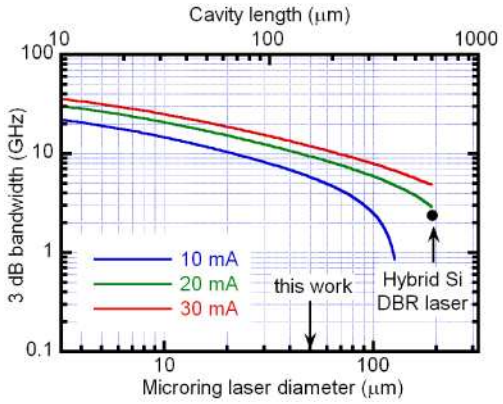

Fig. 6. Calculated 3 dB bandwidth as a function of microring laser diameter (cavity length) for 10, 20 and 30 mA injection current. Black dot represents experimental 3 dB bandwidth of 2.5 GHz measured on a hybrid Si DBR laser without about $1.6 \times I_{th}$ bias current [25].

4. Applications

In the past years a number of companies have announced and started selling active optical cables products [26]. These products are mostly targeted as replacement to existing Infiniband

#115497 - $15.00 USD Received 10 Aug 2009; revised 14 Oct 2009; accepted 20 Oct 2009; published 23 Oct 2009

cables. The main premise of these products is that they can fit into existing infrastructure while providing additional functionality (extended span without repeaters and, possibly lower power consumption) and reducing the system's total cost of ownership. Their appeal mostly resides in the fact that the optical protocol is completely transparent to the user, thus eliminating the need for on-site optical installation.

Most active optical cables use directly modulated VCSELs as the optical engines. VCSELs are likely the most expensive component in the optical module and they present numerous coupling problems. Other companies use CMOS photonics to build modulators and use flip-chip DFB/DBR lasers as optical engine. Once again the lasers and the flip-chip process add cost and potential failure points for these products. Because they need to conform to existing Infiniband protocols, these cables are mostly limited to 10-Gbit/sec (single data rate, or SDR), 20-Gbit/sec (dual data rate, DDR), and 40-Gbit/sec (quad data rate, QDR). Cable lengths are typically of the order of 100 m (300 m for products that use more expensive single longitudinal mode DFB lasers and single-mode fibers).

Future generations of active optical cables will need to meet the increasing bandwidth requirements of peta- and exa-scale computers (i.e. computer systems with 10^{15} to 10^{18} flops) and data centers while keeping costs and complexity low. We believe that the hybrid silicon platform and the microring lasers presented in this paper provide the technology to meet these needs.

A schematic of a possible cable configuration is shown in Fig. 7. The optical engines consist of bundles of microring lasers that are coupled on a single waveguide. The hybrid silicon lasers are designed to emit light at different wavelengths (with a spacing of ~5 nm) and can be directly modulated to create a 10 Gbit/sec on-off keying (OOK) signal. The modulated light from the lasers is coupled into one of the cores of a multicore photonic crystal fiber (PCF) [27]. PCFs together with vertical grating couplers [28] allow high-density connections while reducing the cost of pigtailing the photonic circuit. At the other end of the cable light is coupled onto a second photonic integrated circuit and send to an interleaver-based demultiplexer [29] that separates the various wavelength components and send them to hybrid detectors that recover the data sent. Each fiber core can therefore carry multiple (typically 4-5 for current active medium gain spectrum) 10 Gbit/sec channels in one direction. The fiber consists of up to 19 cores [30] that can be configured (at the hardware level) for up-load or download depending on the traffic needs. This combination of technologies can therefore provide a bandwidth increase of at least one order of magnitude over existing active cables while at the same time reducing complexity and, possibly, cost.

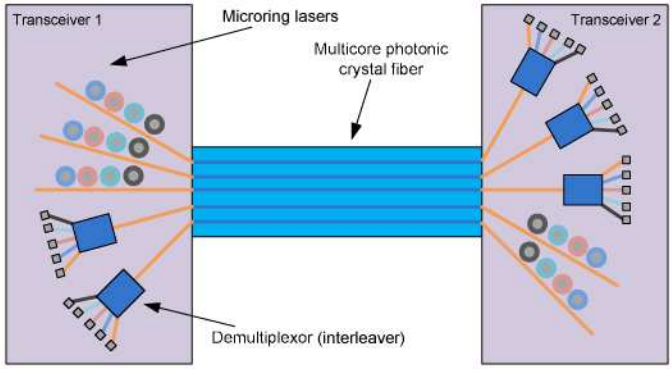

Fig. 7. Schematic view of a CWDM optical cable based on the hybrid silicon platform

5. Conclusion

We have demonstrated electrically-pumped compact microring resonator lasers with integrated photodetectors on a hybrid silicon platform. A new deep-etch, self-aligned fabrication process was developed to enable 50 μm diameter, 2.5 μm wide III-V ring

#115497 - $15.00 USD Received 10 Aug 2009; revised 14 Oct 2009; accepted 20 Oct 2009; published 23 Oct 2009

resonator on a self-aligned Si disk resonator with same dimension. Threshold current as low as 5.4 mA was measured at stage temperature of 10 °C and lasing was observed for temperatures up to 65 °C. Typical threshold power consumption is 10-15 mW at RT (20 °C). Multiple longitudinal mode lasing is observed with major lasing peak at 1528.57 nm aligned with the gain peak which is measured from RT PL. Experimental FSR of 4.2 nm agrees with theoretical calculation for fundamental transverse mode. More than 40 dB extinction ratio and 0.045 nm linewidth (limited by instrument resolution) are measured. A simple IV study reveals that dry etch-exposed active region interface experiences comparable leakage current as wet etch-exposed interface, indicating low surface recombination. Simulated 3 dB bandwidth is 10 GHz for 50 mm diameter microring laser with $4\times I_{th}$ bias current.

The overall device performance meets the basic requirements of small footprint, low power consumption with promising capacity for high-speed modulation. Future devices with smaller diameters and improved processing are expected to result in lower thresholds, higher power and higher temperature operation for optical interconnects.

Acknowledgments

The authors gratefully thank Hui-Wen Chen, Matthew Sysak, Martijn Heck and Mike Haney for valuable discussion and fabrication assistance. We acknowledge the support from HP Innovation Research Program (SBY572738), DARPA Phaser (HR0011-08-1-0347), NSF NNIN REU internship program and NSF funded NNIN fabrication facility at the University of California, Santa Barbara.

#115497 - $15.00 USD Received 10 Aug 2009; revised 14 Oct 2009; accepted 20 Oct 2009; published 23 Oct 2009